Short Communication

Rational Variety Mapping for Contrast-Enhanced Nonlinear Unsupervised Segmentation of Multispectral Images of Unstained Specimen

Ivica Kopriva,* Mirko Hadžija,[†]
Marijana Popović Hadžija,[†] Marina Korolija,[†]
and Andrzej Cichocki[‡§¶]

From the Divisions of Laser and Atomic Research and Development,* and Molecular Medicine,[†] Ruđer Bošković Institute, Zagreb, Croatia; the Laboratory for Advanced Brain Signal Processing,[‡] Brain Science Institute, Saitama, Japan; the Warsaw University of Technology,[§] Warsaw, Poland; and the Systems Research Institute,[¶] Polish Academy of Sciences, Warsaw, Poland

A methodology is proposed for nonlinear contrast-enhanced unsupervised segmentation of multispectral (color) microscopy images of principally unstained specimens. The methodology exploits spectral diversity and spatial sparseness to find anatomical differences between materials (cells, nuclei, and background) present in the image. It consists of rth-order rational variety mapping (RVM) followed by matrix/tensor factorization. Sparseness constraint implies duality between nonlinear unsupervised segmentation and multiclass pattern assignment problems. Classes not linearly separable in the original input space become separable with high probability in the higher-dimensional mapped space. Hence, RVM mapping has two advantages: it takes implicitly into account nonlinearities present in the image (ie, they are not required to be known) and it increases spectral diversity (ie, contrast) between materials, due to increased dimensionality of the mapped space. This is expected to improve performance of systems for automated classification and analysis of microscopic histopathological images. The methodology was validated using RVM of the second and third orders of the experimental multispectral microscopy images of unstained sciatic nerve fibers (nervus ischiadicus) and of unstained white pulp in the spleen tissue, compared with a manually defined ground truth labeled by two trained pathophysiologists. The methodology can also be useful for additional contrast enhancement of images of stained specimens. *(Am J Pathol 2011, 179:547–554; DOI: 10.1016/j.ajpath.2011.05.010)*

Staining of the specimen in the slide preparation process has been standard procedure for many years, because it increases contrast between the cell and the background. However, staining involves hours of preprocessing of the specimen, and can also add chemical effects to the nature of the cells, cause their shrinkage, and alter their morphology.[1] For example, in studying effects of DNA damage on cell viability, fluorescent probes must not be used to stain the cell nuclei, to avoid compromising the viability of the cultures.[2] Similarly, when studying the effects of inhibitor compounds designed to block the replication of cancerous cells, fluorescent dyes must not be used to mark nuclei, because the dyes themselves have toxicity.[3] The subcellular localization of genetically encoded proteins imposes constraints on the cell recognition methods used to draw conclusion about function of a protein; again, staining of the cell is not allowed, to preserve the quality of the specimen and to avoid influencing the result of an investigation.[4] When staining is not allowed, contrast between the cell and the background will be poor, and it is challenging for either a trained pathologist or an automated image processing system to achieve good results. Furthermore, manual classification of cells by trained pathologists in images of stained specimens shows interobserver variability up to 20%.[5] These findings prompted us to explore the possibility of developing a contrast enhancement methodology based on nonlinear unsupervised segmentation of multispectral images with poor contrast between the materials (ie, cells, nuclei, tissue types, and the like) present in the image.

The methodology reported here is based on representation of the multispectral image by a linear mixture model (LMM) in a space induced by rth-order rational variety mapping (RVM), which is a polynomial type of nonlinear mapping.[6] LMM itself has been used in remote sensing for years,[7–9] and recently in medical imaging as well.[10–12] It represents a multispectral image matrix as a product of basis or mixing matrix and matrix of spatial distributions of the materials present in the image (referred to as a source matrix). Very recently, the tensorial nature of the multispectral image has been exploited for the purpose of linear unsupervised segmentation.[13] Thus, any method capable of uniquely factorizing multispectral image matrix or tensor can be used to perform unsupervised segmentation. This implies that only a multispectral image is at disposal for the factorization method. In adopted representation, columns of the basis matrix represent spectral profiles of the materials present in the image.

The quality of linear segmentation depends in the first place on how accurately LMM represents an experimental multispectral image. When nonlinearities are present in the image, accuracy of the LMM-based representation is limited. It can, however, be improved if LMM is used to represent the image in the space induced by the rth-order RVM.[6] This capability is grounded in the duality existing between nonlinear unsupervised image segmentation and pattern recognition problems, such as occurs when spatial distributions of the materials present in the image are mutually sparse. Here, RVM increases the number of separating surfaces between the classes and enables their separability. Then, the multispectral image represents a set of patterns (pixel vectors), columns of the mixing matrix represent centers of the class-related clusters, and sources represent classes. Representing the image by LMM in mapped space has two advantages: it implicitly takes into account the possible presence of nonlinearities in the image (ie, they are not required to be known) and it enhances contrast between spectrally similar materials, which occurs because of increased dimensionality of the mapped space. In this regard, nonlinear band expansion as used by Kopriva and Peršin[10] and by Ouyang et al [14] is a special case (second-order) of the rth-order RVM used in our methodology.

We apply second- and third-order mappings (RVM2 and RVM3, respectively) in combination with several state-of-the-art matrix and tensor factorization methods[15–18] to perform nonlinear unsupervised segmentation of the multispectral microscopy images of the unstained specimen of sciatic nerve fibers (nervus ischiadicus) and spleen tissue. In the first case, our proposed methods yielded significant contrast enhancement between nerve cells and background, relative to segmentation performed by factorization algorithms only. The same outcome occurred in the second experiment: with our proposed methods, lymphatic cells present in the white pulp spleen tissue were better discriminated against the red pulp, relative to segmentation performed by factorization algorithms only. Moreover, RVM3 brought an additional performance improvement. The proposed methodology can also be useful for additional contrast enhancement in analysis and classification problems associated with multispectral images of stained specimens.[19–23] To our knowledge, there is no previous report of nonlinear blind segmentation of multispectral (color) images of either unstained or stained specimens performed by matrix/tensor factorization in the space induced by rth-order RVM.

Materials and Methods

Animal Studies

Adult NOD (10 to 12 weeks old) mice were acquired from the breeding facility at the Ruđer Bošković Institute, Zagreb, Croatia. Animal care and treatment were conducted in conformity with institutional guidelines and in compliance with international law. Before and during the experiments, animals had standard pelleted food and tap water *ad libitum*. The studies were approved by the institutional Ethics Committee.

Histological Analysis

Sciatic nerve fibers and spleen tissue were taken from NOD mice for histological analysis. After extirpation, the tissues were fixed in Bouin's solution for 24 hours. Fixed tissues samples were immersed in increasing concentrations of alcohol for dehydration. After dehydration, tissues were embedded in paraffin. The paraffin blocks were then cut with a microtome into slices 5 μm thick.

Deparaffinization

Microscope glass slides with a histological preparation were put in a rack, covered with foil, and incubated for 5 minutes at 55°C in an oven (Thermo Fisher Scientific, Waltham, MA). Afterwards, glass slides were incubated three times for 15 minutes in toluene. Microscope glass slides with a histological preparation were put in a rack, covered with foil, and incubated for 5 minutes at 55°C in an oven (Thermo Fisher Scientific, Waltham, MA). Afterwards, glass slides were incubated three times for 15 minutes in toluene. Glass slides were then transferred into 100% ethanol at 1 minute, after that started process rehydration for 5 minutes in 96% ethanol, for 5 minutes in 75% ethanol, and for two 5-minute washes in distilled water with constant stirring.

Preparation for Staining and Antigen Retrieval

Deparaffinized microscope glass slides with histological preparation were placed in a rack, plunged into 450 mL citrate buffer, and heated two times for 5 minutes in a microwave oven. Slides were then transferred into hot water, heated to 60°C, and stored until cooled down to room temperature. After cooling, slides were washed three times for 5 minutes in PBS buffer at room temperature.

Staining

The microscopic glass slides with histological preparation were applied to 50 μL incubation buffer. After incubation and mixing (for 30 minutes) glass slides were washed with PBS buffer. On each slide, 50 μL primary monoclonal antibody (mAb IgG) was added and slides were incubated for 60 minutes with occasional mixing. After incubation, the slides were rinsed thoroughly three times for 5 minutes in PBS buffer. Next, 80 μL 10% glycerol-PBS was added to each slide; slides were then coverslipped. Finally, processed glass slides were analyzed under a microscope.

Multispectral Microscope Image Acquisition

Spectral images of the slides were acquired at room temperature, in the 10% glycerol-PBS imaging medium, under an Olympus BX51 fluorescence microscope (Olympus America) equipped with a DP50 camera (numerical aperture of the objective lens, 1/120; Olympus Singapore), at $\times$400 magnification, and with Viewfinder Lite 1.0 image acquisition software (Better Light, Inc., San Carlos, CA). Preparations were scanned using spectral filters at wavelengths of 465, 510, 578, and 620 nm. Acquired spectral images were analyzed in a MATLAB software environment with programs written in MATLAB script language (Mathworks, Natick, MA).

Multispectral Image and Linear Mixture Model

The multispectral image of a specimen is represented by the LMM in a space induced by rth-order RVM (see Cover[6]), $\phi(\mathbf{X})$ (the mapping itself is formally defined in the next section):

$$\phi(\mathbf{X}) \approx \mathbf{A}_\phi \phi(\mathbf{S}) \qquad (1)$$

where $\mathbf{X} \in R_{0+}^{I_3 \times I_1 I_2}$ stands for the multispectral image comprised of I_3 spectral bands and $I_1 \times I_2$ pixels and $\mathbf{S} \in R_{0+}^{J \times I_1 I_2}$ stands for the matrix of sources representing spatial distributions of J materials present in the image. The first-order mapping represents the original image itself, and model (1) becomes a standard LMM in the original input space, $\mathbf{X} \approx \mathbf{A}\mathbf{S}$, used commonly in multispectral image analysis,[7–11] where $\mathbf{A} \in R_{0+}^{I_3 \times J}$ stands for a matrix of spectral profiles of J materials present in the image. In mapped space, $\phi(\mathbf{X}) \in R_{0+}^{\bar{I}_3 \times I_1 I_2}$ and $\mathbf{A}_\phi \in R_{0+}^{\bar{I}_3 \times \bar{J}}$, where $\bar{I}_3 > I_3$ and $\bar{J} > J$. Hence, RVM has dimensionality (band) expansion effect. In the image segmentation problem considered, $\phi(\mathbf{X})$, $\mathbf{A}_\phi$, and $\phi(\mathbf{S})$ are assumed to be nonnegative. Matrix representation (1) is obtained from three-dimensional multispectral image tensor $\underline{\mathbf{X}} \in R_{0+}^{I_1 \times I_2 \times I_3}$ by row or column stacking procedures.

To obtain factorization (1) unique up to permutation and scaling indeterminacies, which are inherent to blind decompositions, sparseness constraints are imposed by non-negative matrix factorization (NMF) algorithms[24] or statistical independence constraints are imposed by independent component analysis (ICA) algorithms[25] on rows of $\phi(\mathbf{S})$. Sparseness implies that one material dominantly occupies each pixel footprint, and that condition is fulfilled for histopathological images of the specimen. The statistical independence assumption fails when materials are spectrally similar. This occurs, for example, in the case of low-dimensional multispectral imaging of a skin tumor with a low fluorescence intensity,[10,11] but occurs also with multispectral microscopy imaging of an unstained specimen with low contrast between the cell and the background.

An alternative to matrix representation of multispectral image is tensor representation $\underline{\mathbf{X}} \in R_{0+}^{I_1 \times I_2 \times I_3}$ (see Ref. 13), with elements $\{x_{i_1 i_2 i_3}\}_{i_1, i_2, i_3=1}^{I_1, I_2, I_3}$; that is, the multispectral image is a set of I_3 spectral band images with the size of $I_1 \times I_2$ pixels. This is a standard notation adopted for use in multiway analysis.[26] For the purpose of multispectral image decomposition, a Tucker3 tensor model is adopted[27]:

$$\phi(\underline{\mathbf{X}}) \approx \underline{\mathbf{G}}_\phi \times_1 \mathbf{A}_\phi^{(1)} \times_2 \mathbf{A}_\phi^{(2)} \times_3 \mathbf{A}_\phi^{(3)} \qquad (2)$$

where, as in model (1), the image is represented in the mapped space and first-order mapping of ϕ yields two-dimensional LMM in the original space,[13] thus: $\underline{\mathbf{X}} \approx \underline{\mathbf{G}} \times_1 \mathbf{A}^{(1)} \times_2 \mathbf{A}^{(2)} \times_3 \mathbf{A}^{(3)}$. Here, $\underline{\mathbf{G}} \in R_{0+}^{J \times J \times J}$ is a core tensor, $\{\mathbf{A}^{(n)} \in R_{0+}^{I_n \times J_3}\}_{n=1}^{3}$ are factors, and x_n denotes n-mode product of a tensor with a matrix $\mathbf{A}^{(n)}$. In mapped space, the dimension that corresponds to spectral mode I_3 is replaced by induced dimension $\bar{I}_3$, where $\bar{I}_3 > I_3$. In tensor model (2), array factor $\mathbf{A}_\phi^{(3)}$ corresponds to the matrix of spectral profiles $\mathbf{A}_\phi$ in model (1).[13] In contrast to matrix factorization model (1), tensor factorization model (2) exploits spatial structure of the multispectral image and enables decomposition in which uniqueness does not depend on the fulfillment of hard constraints on model factors such as sparseness or statistical independence.[18,24] Furthermore, spatial distributions of the materials present in the image (cell and background) are immediately obtained in tensor format[13]:

$$\phi(\underline{\mathbf{S}}) \approx \phi(\underline{\mathbf{X}}) \times_3 (\mathbf{A}_\phi^{(3)})^\dagger \qquad (3)$$

where $\phi(\underline{\mathbf{S}}) \in R_{0+}^{I_1 \times I_2 \times J}$ and $\dagger$ denotes the Moore-Penrose pseudo-inverse.

Contrast Enhancement of Unstained Specimen by Rational Variety Mapping

With LMM-based representation of the multispectral image, it is apparent that contrast enhancement between the materials occurs when the angle between their spectral profiles (column vectors in the mixing matrix) is increased. This coincides with increased dimensionality of the space induced by rth-order RVM. The nonlinear band expansion, introduced in Refs. 10, 14, and 28, is just a special case (corresponding to $r = 2$) of the rth-order RVM. The rth-order RVM of the pixel vector pattern $\mathbf{x} \in R_{0+}^{I_3}$ at spatial coordinate $i_1 i_2$ is of the form

$$\phi(\mathbf{x}) = \left[1 \{ x_1^{q_1} x_2^{q_2} \times \cdots \times x_{I_3}^{q_{I_3}} \}_{q_1, \dots, q_{I_3}=0}^{r} \right]^\top \text{ s.t.}$$
$$0 < \sum_{i_3=1}^{I_3} q_{i_3} \leq r \qquad (4)$$

That is, it involves monomials up to the order r. It increases dimensionality of the pattern from l_3 to $\bar{l}_3 = \binom{l_3+r}{r} = \frac{(l_3+r)!}{l_3!r!}$. This, for $l_3 = 4$ spectral images used in the experiments reported here yields $\bar{l}_3 = 15$ for RVM2 and $\bar{l}_3 = 35$ for RVM3. This enables separability between mapped patterns with high probability, because the number of separating surfaces grows with r and is given with

$$C(l_1 l_2, d) = 2 \sum_{k=0}^{d-1} \binom{l_1 l_2 - 1}{k},$$

where $d = (l_3 + r)!/l_3!r!$ [see equation (5) in Ref. 6]. However, computational complexity grows rapidly when r increases, and therefore second-order or perhaps third-order RVM are of primary practical interest. From the standpoint of pattern separability, order of the RVM depends on the strength of nonlinearities present in the image. Hence, it is probable that performance improvement brought by higher-order RVM will be small, compared with the increase in computational complexity. Nevertheless, RVM enables nonlinear blind multispectral image decomposition, wherein nonlinearities do not need to be known. Because of increased dimensionality of the mapped space, RVM also improves the contrast between spectrally similar materials (as for unstained specimen images, for which contrast is low). Nonetheless, it is important to note that factorization of the LMM of models (1) and/or (2) in mapped space does not immediately lead to the solution of the segmentation problem. That is because $\phi(\mathbf{S})$ in (1) resembles $\phi(\mathbf{X})$ in (4), implying that actual solutions $\{s_j\}_{j=1}^{J}$ are hidden among many spurious ones. However, mutual sparseness con-
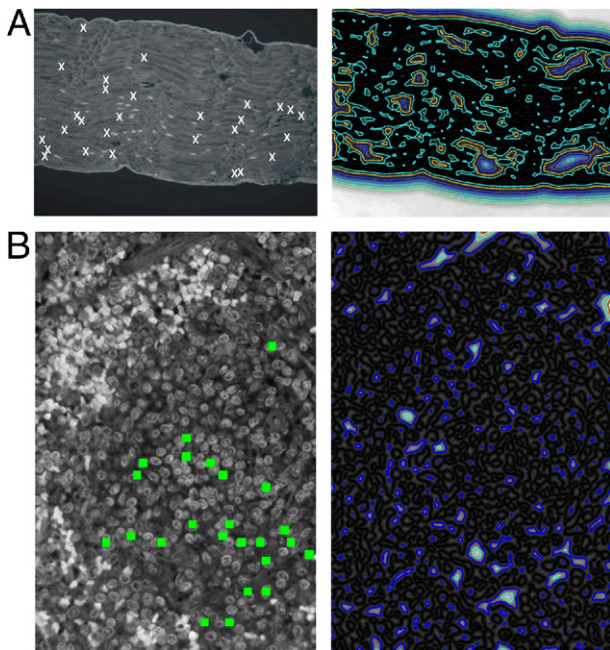

Figure 1. Spectral fluorescent microscopy images at 510 nm of histological slices of unstained specimens of sciatic nerve fibers (nervus ischiadicus) (**A**) and spleen (**B**). False-positive predicted nerve fiber spots (**A**) are marked by **white crosses** and false-positive predicted lymph nodes in the spleen tissue (**B**) are marked by **green squares**. **Left**: Spectral image. **Right**: Isolines of the estimated energy of the vector field convolution (VFC).
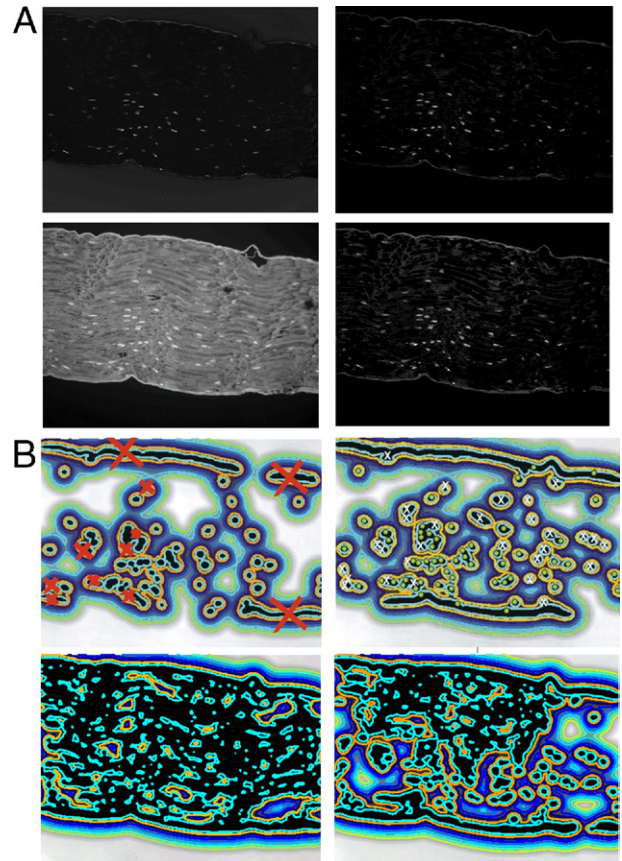

Figure 2. Segmented images of sciatic nerve fibers (**A**) with corresponding isolines of the estimated external energy of the VFC (**B**). **Left**: Second-order RVM2 and DCA algorithm. **Right**: Third-order RVM3 and NMU-ℓ_1 algorithm. Isoline images in B are obtained from segmented images shown in A and are in one-to-one correspondence with them. On the isoline images obtained from the RVM-transformed images, the false-positive and false-negative spots are marked by **red or white crosses**, respectively; spots that fall on tissue border were excluded from the accuracy analysis.

straint simplifies $\phi(\mathbf{S})$, because all of the monomials that involve cross-products vanish and $\phi(\mathbf{S})$ becomes

$$\phi(\mathbf{s}) = \left[1\, s_1 s_1^2 ... s_1^r .... s_J s_J^2 ... s_J^r\right]^{\mathsf{T}} \quad (5)$$

where T denotes transpose. Now, sparseness-based factorization enforces factorization: $\phi(\mathbf{s}) = \left[1\bar{s}_1 ... \bar{s}_J\right]^{\mathsf{T}}$ where $\bar{s}_j = \sum_{q=1}^{r} s_j^q$, $j = 1,... ,J$, represent equivalent sources that are mutually sparse (although different powers of the same source are not). For image segmentation this solution is legitimate, because any combination of the powers of the spatial distributions of the material is itself a spatial distribution of the material.

Factorization Methods for Unsupervised Segmentation of Multispectral Image

Here, we briefly review four state-of-the-art methods for factorization of matrix (1) and tensor (2) models of the multispectral image of a principally unstained specimen. These methods are referred to as i) dependent component analysis (DCA),[10,11] ii) multilayer hierarchical alternating least-square non-negative matrix factorization

Table 1. Outcomes for Image Analysis of the Unstained Specimen and of Images Segmented by the Different Transforms and Algorithms

Outcome	Unstained specimen	RVM2 DCA	RVM3 DCA	RVM2 β-NTF	RVM3 β-NTF	RVM2 HALS NMF	RVM3 HALS NMF	RVM2 NMU-ℓ_1	RVM3 NMU-ℓ_1
Sciatic nerve fiber (nervus ischiadicus)									
N_{TP}	55/55	50/51	52/51	48/48	53/55	50/49	54/54	48/49	58/58
N_{FN}	0/0	4/4	4/2	5/5	2/1	5/55	1/2	4/4	1/1
N_{FP}	27/27	11/11	30/32	20/19	42/40	20/22	20/19	27/25	29/30
Spleen tissue									
N_{TP}	128/131	128/131	126/121	128/131	Failed	128/131	Failed	128/131	118/117
N_{FN}	0/0	3/7	3/5	3/6	Failed	5/5	Failed	5/8	2/1
N_{FP}	55/47	41/48	24/23	24/33	Failed	31/25	Failed	29/35	17/19

Results obtained independently by two pathologists are separated by a virgule mark.

Transforms: RVM2 and RVM3 (second-order and third-order rational variety mapping). Algorithms: DCA (dependent component analysis), β-NTF (β-divergence non-negative tensor factorization), HALS NMF (hierarchical alternating least-square non-negative matrix factorization), and NMU-$\ell1$ (non-negative matrix underapproximation).

N_{FN}, number of false negatives; N_{FP}, number of false positives; N_{TP}, number of true positives.

(HALS NMF),[16,17] iii) non-negative matrix underapproximation (NMU),[15] and iv) non-negative tensor factorization (NTF).[18]

DCA is an extension of independent component analysis for problems in which statistical independence assumption between sources is not fulfilled. Then, high-pass filtering based preprocessing transform T is applied on multispectral image (1), yielding $T(\phi(\mathbf{X})) = \mathbf{A}_\phi T(\phi(\mathbf{S}))$, whereupon rows of $T(\phi(\mathbf{S}))$ are more statistically independent than rows of $\phi(\mathbf{S})$. ICA algorithms are then applied to $T(\phi(\mathbf{X}))$, yielding more accurate estimation of $\mathbf{A}_\phi$. Afterward, sources are recovered through $\phi(\mathbf{S}) \approx (\mathbf{A}_\phi)^\dagger \phi(\mathbf{X})$. Candidates for preprocessing transform T include wavelet packets,[29] filter banks,[30] and innovations.[31]

The HALS NMF algorithm minimizes global cost function $D(\phi(\mathbf{X})\|\mathbf{A}_\phi\phi(\mathbf{S})) = \|\phi(\mathbf{X}) - \mathbf{A}_\phi\phi(\mathbf{S})\|_2^2$ to estimate mixing matrix $\mathbf{A}_\phi$, and a set of local cost functions $D(\phi(\mathbf{X}^{(j)})\|\mathbf{a}_{\phi;j}\phi(\underline{s_j})) = \|\phi(\mathbf{X}^{(j)}) - \mathbf{a}_{\phi;j}\phi(\underline{s_j})\|_2^2$, $j = 1,...,J$, to estimate the sources $\{\phi(\underline{s_j})\}_{j=1}^J$, where $\phi(\mathbf{X}^{(j)}) = \phi(\mathbf{X}) - \sum_{k\neq j} \mathbf{a}_{\phi;k}\phi(\underline{s_k})$ and underlining denotes the row vectors. To obtain factorization unique up to permutation and scaling, sparseness constraints are imposed on $\{\underline{\mathbf{s}_j}\}_{j=1}^{\bar{J}}$.[17,12] As already noted, they enforce all of the powers of the same source to combine into one equivalent source: $\{\underline{\mathbf{s}_j}\}_{j=1}^J \rightarrow \{\underline{\mathbf{s}_j}\}_{j=1}^J$. An additional performance improvement of the NMF algorithms is obtained when they are applied in the multilayer mode.[16]

The NMU has been introduced recently as a refinement of the NMF algorithms toward sparse factorization of $\phi(\mathbf{X})$ in (1). In addition to non-negativity constraints imposed on $\mathbf{A}_\phi$ and $\phi(\mathbf{S})$, the cost function $D(\phi(\mathbf{X})\|A_\phi\phi(\mathbf{S})) = \|\phi(\mathbf{X}) - A_\phi\phi(\mathbf{S})\|_2^2$ is minimized, imposing an underapproximation constraint on $\mathbf{A}_\phi$ and $\phi(\mathbf{S})$: $A_\phi\phi(\mathbf{S}) \leq \phi(\mathbf{X})$. This naturally generates a sparse solution without imposing direct constraints on the rows of $\phi(\mathbf{S})$. Thus, problems associated with selection of optimal values of the regularization constants and/or number of layers are avoided. Depending on the norm of the cost function, NMU algorithm can be used in two versions: NMU-l2 if l2 norm is used, and NMU-l1 if l1 norm is used. Code for the NMU algorithm as used for image segmentation in the present study is available at *http://www.core.ucl.ac.be/~ngillis/papers/recursiveNMU.m*.

The NTF algorithms are based on minimization of a chosen discrepancy measure between multispectral image tensor $\phi(\underline{\mathbf{X}})$ and its model (2). Discrepancy measures based on α- and β-divergences have been used recently, because of their adaptability to data statistics.[24] Results related to unsupervised segmentation of the multispectral microscopy images of unstained specimens of nerve cells and spleen tissues reported here were obtained by an NTF algorithm that minimizes the β-divergence between $\phi(\underline{\mathbf{X}})$ and its model $\phi(\underline{\widehat{\mathbf{X}}})$. For equations of the multiplicative NTF algorithms based on β-divergence, as well as α-diver-

Table 2. Sensitivity and Positive Predictive Value of Image Analysis of the Unstained Specimen and of Images Segmented by the Different Transforms and Algorithms

Statistic*	Unstained specimen	RVM2 DCA	RVM3 DCA	RVM2 β-NTF	RVM3 β-NTF	RVM2 HALS NMF	RVM3 HALS NMF	RVM2 NMU-ℓ_1	RVM3 NMU-ℓ_1
Nerve fiber (nervus ischiadicus)									
Sens, %	100/100	**92.6/92.7**	92.9/96.2	90.6/90.6	96.4/98.2	90.9/90.7	**98.2/96.4**	92.3/92.5	98.3/98.3
PPV, %	67/67	**82/82.3**	63.4/61.4	70.6/71.6	55.8/57.9	71.4/69	**73/74**	64/66.2	66.7/65.9
Spleen tissue									
Sens, %	97.7/97.7	97.7/94.9	**97.7/96**	97.7/95.6	Failed	96.2/96.3	Failed	96.2/94.2	**98.3/99.2**
PPV, %	70/73.6	75.7/73.2	**84/84**	84.2/79.9	Failed	80.5/84	Failed	81.5/78.9	**87.4/86**

Results obtained independently by two pathologists are separated by a virgule mark. Bold type indicates the several best results that combine high sensitivity and low false positive alarm rate.

*Sens = $N_{TP}/(N_{TP} + N_{FN})$ and PPV = $N_{TP}/(N_{TP} + N_{FP})$, where Sens is sensitivity, N is number, TP is true positive, FN is false negative, FP is false positive, and PPV is positive predictive value.

gence, we refer the reader to Ref. 18 and to sections 7.4.4 and 7.4.5 in Ref. 24.

Results

Contrast enhancement capability of the RVM-based methods was demonstrated on one multispectral fluorescent image of the unstained specimen of sciatic nerve fibers and one of the spleen tissue. Recorded multispectral images comprised four spectral images at 465, 510, 578, and 620 nm; 510 nm is the wavelength at which the best contrast was obtained; Figure 1A shows the 510-nm spectral image of unstained sciatic nerve fibers, and Figure 1B shows the cross-section of unstained spleen tissue. The cross-section of the spleen shows both red and white pulp; the white pulp consists further of lymph nodes or follicles. The image also shows a part of the spleen that is wrapped around the white pulp. This part consists of reticular fibers and is full of red blood cells. Part of the white pulp, which is of interest to our research, shows diffuse lymph tissue that belongs to the family of T lymphocytes.

Two pathophysiologists (M.H. and M.P.H.) evaluated these images. In the image of unstained sciatic nerve fibers, both pathophysiologists detected 55 true-positive nerve fiber spots and 28 false-positive spots (Figure 1A). It is of greater importance, however, that an automated recognition would be highly unreliable because of weak contrast between the nerve spots and the background. This is demonstrated in Figure 1A, which shows isolines of the estimated external energy of the vector field convolution (VFC),[32,33] calculated for the 510-nm spectral image of the unstained specimen. Because of weak boundaries, isolines are not closed around the spots but are scattered randomly across the image. Figure 2A shows images segmented from multispectral image of unstained specimen by the RVM2 transform and DCA algorithm and by the RVM3 transform and NMU-ℓ_1 algorithm, with corresponding images obtained without RVM transform. Isolines of the estimated external energy (Figure 2B) are shown in one-to-one correspondence with their related images (Figure 2A).

The most important finding is that contrast enhancement due to the use of the RVM yielded stronger boundaries of the nerve fiber spots, and these are, therefore, better encircled by isolines. This enables more accurate classification and/or analysis of histopathological microscopy images. This statement is further supported by quantitative performance analysis performed by the two trained pathophysiologists (M.H. and M.P.H.). The numbers of true-positive (N_{TP}), false-positive (N_{FP}), and false-negative (N_{FN}) outcomes are reported in Table 1 for the unstained image and for images segmented by the RVM2 and RVM3 transforms paired with DCA, β-NTF, HALS NMF, and NMU-ℓ_1 algorithms. Table 2 reports sensitivity and positive predictive value. In the validation phase, the attention of the pathophysiologists was on the spots encircled by isolines, which would normally be checked by an automated classification system. Where a false positive or false negative fell in a part of the specimen corre-
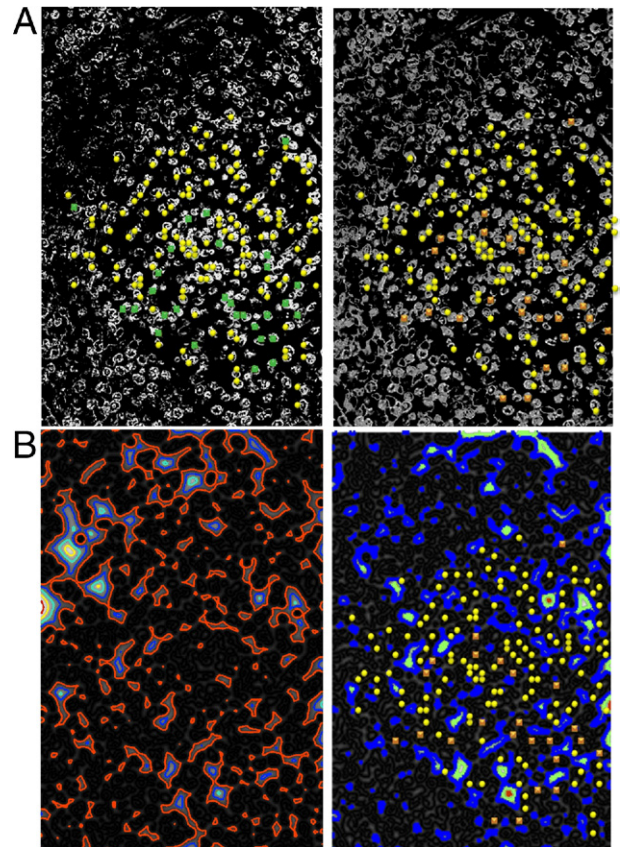

Figure 3. Segmented images of spleen tissue (**A**), with corresponding isolines of the estimated external energy of the VFC (**B**). **Left**: Second-order RVM2 NMU-ℓ_1 algorithm. **Right**: Third-order RVM3 and NMU-ℓ_1 algorithm. True-positive spots are marked with **yellow circles**. False-negative spots are marked with **green squares** in the second-order RVM2 NMU-ℓ_1 segmented image and with **orange squares** in the third-order RVM3 NMU-ℓ_1 segmented image.

sponding to a border line (Figure 2B), it was excluded from the accuracy analysis (Table 2).

The RVM2-DCA method yielded the smallest false-alarm rate (PPV $\approx$ 82.1%, with sensitivity (Sens) $\approx$ 92.6%; Table 2), which is significantly better than the rate obtained from the image of the unstained specimen. The highest accuracy (Sens $\approx$ 97.3%) was obtained with the RVM3-HALS NMF algorithm, but with increased false-alarm rate. Overall, the RVM2-DCA would be the method of choice for the present example. It is also important to note that, for the case of sciatic nerve fiber, the interobserver variability was small; the worst case was 3% for images segmented by RVM3-DCA and RVM2 NMU-ℓ_1 algorithms. Figure 3 shows results obtained by the RVM2 and RVM3 transforms and NMU-ℓ_1 algorithm, with corresponding isolines. Red blood cells located in the upper left corner are suppressed and the white pulp part of the spleen tissue is emphasized (Figure 3A). For a reference, an image of the unstained specimen and the corresponding isolines are shown in Figure 1B. Because of weak boundaries, isolines are scattered randomly across the image for the unstained specimen (Figure 1). Isolines shown in Figure 3B show more regular structure.

Quantitative performance analysis was conducted by two pathophysiologists. The numbers of true-positive

(N_{TP}), false-positive (N_{FP}), and false-negative (N_{FN}) outcomes are reported in Table 1, and the sensitivity and positive predictive values are reported in Table 2. RVM3 paired with β-NTF and HALS NMF methods failed to detect true-positive spots in spleen tissue. These methods were therefore excluded from the accuracy analysis (Table 2). The failure was a consequence of significantly increased computational complexity of RVM3 and β-NTF/HALS NMF; it takes many hours to segment the image, and selection of the optimal values of free parameters becomes intractable. On the other hand, segmentation by RVM3 and DCA/NMU was performed within several minutes.

All methods yielded consistent improvement of false-alarm rate ($\geq$10% improvement), relative to the case of image of unstained specimen (Table 2). Moreover, RVM3-NMU yielded the smallest false-alarm rate (PPV $\approx$ 86.7%) and the best accuracy (Sens $\approx$ 98.7%). In the present study, RVM3 brought additional performance improvement over RVM2, as did the RVM3-DCA algorithm.

Discussion

A contrast-enhancement methodology is proposed for nonlinear unsupervised segmentation of fluorescent multispectral microscopy images of unstained specimens. The methodology combines rth-order RVM, to increase spectral diversity between the materials present in the image, with non-negative matrix or tensor factorization. The methodology was demonstrated on images of unstained specimen of sciatic nerve fiber and spleen tissue. Lymphatic cells present in the spleen tissue were visually and anatomically clearly separated from their envelopes of red pulp. The results obtained imply that staining of the specimen only for contrast enhancement can be avoided, enabling the specimen to be used for visual inspection by a pathophysiologist, as well as for other purposes that require absence of staining. Moreover, the demonstrated contrast-enhancement enables design of an automated system for classification and analysis of unstained microscope histopathological images. RVM-based nonlinear blind image segmentation has two main advantages: it implicitly takes into account the possibly nonlinear nature of the image and it enhances contrast between spectrally similar materials, which occurs because of increased dimensionality of the mapped space. It is conjectured that a theoretical framework related to reproducible kernel Hilbert space will further be relevant for this purpose.

References

1. Lai C, Khosla R: GA based optimisation of a multi-agent soft computing model for segmentation and classification of unstained mammalian cell images. Proceedings of the 2003Congress of Evolutionary Computation 2003 (CEC 2003), 8–12 Dec. 2003, Canberra, Australia. IEEE Computer Society Press, Los Alamitos, CA, 2003, 2:1192–1198. doi: 10.1109/CEC.2003.1299804.
2. Lupica G, Allinson NM, Botchway SW: 2008. Hybrid image processing technique for robust identification of unstained cells in bright-field microscope images. Proceedings of the 2008International Conferences on Computational Intelligence for Modelling, Control and Automation; Intelligent Agents, Web Technologies and Internet Commerce; and Innovation in Software Engineering (CIMCA 2008, IAWTIC 2008, and ISE 2008), Vienna, Austria, Dec. 10–12, 2008. IEEE Computer Society Press, Los Alamitos, CA, 2008, 1:1053–1058. doi: 10.1109/CIMCA.2008.144.
3. Padfield DR, Rittscher J, Sebastian T, Thomas N, Roysam B: Spatiotemporal cell cycle analysis using 3D level set segmentation of unstained nuclei in line scan confocal fluorescence images. Proceedings of the 2006 IEEE International Symposium on Biomedical Imaging: From Nano to Macro (ISBI 2006), Arlington, VA, April 6–9, 2006. IEEE Computer Society Press, Los Alamitos, CA, 2006, 1:1036–1039[doi: 10.1109/ISBI.2006.1625098]
4. Tscherepanow M, Jensen N, Kummert F. Recognition of Unstained Live Drosophila Cells in Microscope Images. IEEE International Machine Vision and Image Processing Conference (IMVIP 2007), Maynooth, Ireland, Sept. 5–7, 2007. IEEE Computer Society Press, Los Alamitos, CA, 2007, 1:169–176. doi: 10.1109/IMVIP.2007.16
5. Erasmus JJ, Gladish GW, Broemeling L, Sabloff BS, Truong MT, Herbst RS, Munden RF. Interobserver and intraobserver variability in measurement of non-small-cell carcinoma lung lesions: implications for assessment of tumor response. J Clin Oncol 2003, 21:2574–2582
6. Cover TM: Geometrical and statistical properties of systems of linear inequalities with applications in pattern recognition. IEEE Trans Elect Comput 1965, EC-14:326–334
7. Adams JB, Smith MO, Johnson PE: Spectral mixture modeling: a new analysis of rock and soil types at the Viking Lander 1 suite. J Geophys Res 1986, 91:8098–8112
8. Settle JJ, Drake NA: Linear mixing and estimation of ground cover proportions. Int J Remote Sens 1993, 14:1159–1177
9. Craig M: Minimum-volume transforms for remotely sensed data. IEEE Trans Geosci Remote Sens 1994, 32:542–552
10. Kopriva I, Peršin A: Unsupervised decomposition of low-intensity low-dimensional multi-spectral fluorescent images for tumour demarcation. Med Image Anal 2009, 13:507–518
11. Kopriva I, Peršin A, Puizina-Ivić N, Mirić L: Robust demarcation of basal cell carcinoma by dependent component analysis-based segmentation of multi-spectral fluorescence images. J Photochem Photobiol B 2010, 100:10–18
12. Kopriva I, Cichocki A: Blind decomposition of low-dimensional multi-spectral image by sparse component analysis. J Chemometrics 2009, 23:590–597
13. Kopriva I, Cichocki A: Blind multispectral image decomposition by 3D nonnegative tensor factorization. Opt Lett 2009, 34:2210–2212
14. Ouyang YC, Chen HM, Chai JW, Chen CCC, Poon SK, Yang CW, Lee SK, Chang CI: Band expansion-based over-complete independent component analysis for multispectral processing of magnetic resonance image. IEEE Trans Biomed Eng 2008, 55:1666–1677
15. Gillis N, Glineur F: Using underapproximations for sparse nonnegative matrix factorization. Pattern Recog 2010, 43:1676–1687
16. Cichocki A, Zdunek R: Multilayer nonnegative matrix factorization. Electron Lett 2006, 42:947–948
17. Cichocki A, Zdunek R, Amari SI: Hierarchical ALS algorithms for nonnegative matrix factorization and 3D tensor factorization. Independent Component Analysis, ICA07, London, UK, Sept. 9–12, 2007. Lecture Notes Comput Sci 4666. Berlin, Springer, 2007, 169–176
18. Cichocki A, Phan AH: Fast local algorithms for large scale nonnegative matrix and tensor factorizations. IEICE Trans Fundamentals 2009, E92]?>-A708–721
19. Zimmer C, Labruyère E, Meas-Yedid V, Guillén N, Olivio-Marin JC: Segmentation and tracking of migrating cells in videomicroscopy with parametric active contours: a tool for cell-based drug testing. IEEE Trans Med Imaging 2002, 21:1212–1221
20. Arambula Cosio F, Márquez Flores JA, Padilla Castañeda MA, Solano S, Tato P: Automatic counting of immunocytochemically stained cells. Engineering in Medicine and Biology Society, 2003. Proceedings of the 25th Annual International Conference of the IEEE, Cancun, Mexico, Sept. 17–21, 2003. IEEE Computer Society Press, Los Alamitos, CA, 2003, 1:790–793. doi: 10.1109/IEMBS.2003.1279883
21. Masmoudi H, Hewitt SM, Petrick N, Myers KJ, Gavrielides MA: Automated quantitative assessment of HER-2/neu immunohistochemical expression in breast cancer. IEEE Trans Med Imaging 2009, 28:916–925

22. Mao KZ, Zhao P, Tan PH: Supervised learning-based cell image segmentation for p53 immunohistochemistry. IEEE Trans Biomed Eng 2006, 53:1153–1163

23. Arif M, Rajpoot N: Classification of potential nuclei in prostate histology images using shape manifold learning. International Conference on Machine Vision (ICMV 2007), Islamabad, Pakistan, Dec. 28–29, 2007. IEEE Computer Society Press, Los Alamitos, CA, 2007, 1:113–118. doi: 10.1109/ICMV. 2007.4469283

24. Cichocki A, Zdunek R, Phan AH, Amari SI: Alternating Least Squares and Related Algorithms for NMF and SCA Problems. Nonnegative Matrix and Tensor Factorizations: Applications to Exploratory Multi-Way Data Analysis and Blind Source Separation, ch 4. Chichester, UK, John Wiley, 2009, pp 203–266

25. Cichocki A, Amari SI: Adaptive Blind Signal and Image Processing. Chichester, UK, John Wiley, 2002, pp 129–174, 231–233

26. Kiers HAL: Towards a standardized notation and terminology in multiway analysis. J Chemometrics 2000, 14:105–122

27. Tucker RL: Some mathematical notes on three-mode factor analysis. Psychometrika 1966, 31:279–311

28. Du Q, Kopriva I, Szu H: Independent component analysis for classifying multispectral images with dimensionality limitation. Int J Inf Acquis 2004, 1:201–216

29. Kopriva I, Seršić D: Wavelet packets approach to blind separation of statistically dependent sources. Neurocomputing 2008, 71:1642–1655

30. Tanaka T, Cichocki A: Subband decomposition independent component analysis and new performance criteria. Proceedings of the IEEE Conference on Acoustics, Speech, and Signal Processing, 2004(ICASSP '04). IEEE Computer Society Press, Los Alamitos, CA, 2004, 5:541–544

31. Hyvärinen A: Independent component analysis for time-dependent stochastic processes. Proceedings of the International Conference on Artificial Neural Networks (ICANN '98) 1998, Skovde, Sweden, Sept. 2–4, 1998. Berlin, Springer, 1998, 1:541-546

32. Li B, Acton ST: Active contour external force using vector field convolution for image segmentation. IEEE Trans Image Process 2007, 16:2096–2106

33. Li B, Acton ST: Automatic active model initialization via Poisson inverse gradient. IEEE Trans Image Process 2008, 17:1406–1420